

Turbulence strength estimation from an arbitrary set of atmospherically degraded images

Steve Zamek and Yitzhak Yitzhaky

Department of Electro-Optics Engineering, Ben Gurion University, P.O. 653, Beer Sheva 84105, Israel

Received February 9, 2006; revised June 6, 2006; accepted June 26, 2006; posted July 10, 2006 (Doc. ID 67867)

In remote sensing, atmospheric turbulence and aerosols usually limit the image quality. For many practical cases, turbulence is shown to be dominant, especially for horizontal close-to-earth imaging in hot environments. In a horizontal long-range imaging, it is usually impractical to calculate path-averaged refractive index structure constant C_n^2 (which characterizes the turbulence strength) with conventional equipment. We propose a method for estimating C_n^2 from the available atmospherically degraded video sequence by calculating temporal intensity fluctuations in spatially high variance areas. Experimental comparison with C_n^2 measurements using a scintillometer shows reliable estimation results. © 2006 Optical Society of America

OCIS codes: 010.1330, 030.6600, 010.1290.

1. INTRODUCTION

Inhomogeneities in the atmosphere cause refractive index variations according to various meteorological parameters such as temperature and humidity.¹ These fluctuations lead to random refractions of the light beam propagating through the atmosphere. Hence, the light is received in a large variety of angles of incidence at the optical aperture. In imaging through a long atmospheric path, this phenomenon strongly affects image quality, mainly by means of spatial blur and spatiotemporal image distortions ("image dancing").

The main techniques for the correction of turbulence-caused image degradation are adaptive optics and image processing. Adaptive optics is mainly applied in large telescopes and processes the image in real time.² However, it requires a reference point source that is usually unavailable in horizontal imaging. Image processing includes image restoration^{3,4} and superresolution^{5,6} techniques. Image restoration basically applies digital filtering techniques to deblur the degraded image. The turbulence blurring modulation transfer function (MTF) required for the image restoration process can be defined by the refractive index structure constant,⁷ C_n^2 .

Various measurement instruments and techniques have been proposed for horizontal C_n^2 evaluation. These include scintillation detection and ranging⁸ (SCIDAR), slope detection and ranging^{9,10} (SLODAR), differential image motion¹¹ (DIM), classical scintillometer,^{12,13} and others.¹⁴ Scintillometry, for instance, requires a sender-receiver setup that significantly limits potential applications of the method. The drawback of these techniques is their use of bulky and expensive equipment. Another way to estimate the value of C_n^2 is to place, at the object plane, a point source (such as a laser) or an artificial target such as a point, a bar, or a step edge, from which the angle of arrival fluctuations can be calculated.^{15,16} However, these techniques are usually not practical in real-life long-distance horizontal imaging. The blurring MTF can be estimated from an already existing step edge in the image;⁴

but such a specific knowledge about the structure of the image is confined to limited types of images, as a well-structured step edge may not exist in the common scenario.

In this paper, we propose a method for C_n^2 estimation given only the available recorded turbulent-degraded image sequence. The method exploits the turbulence-induced spatiotemporal movements across the frames of the image set, together with the spatial properties of real images, to estimate the angle-of-arrival (AOA) obtained from different areas in the image. C_n^2 can then be extracted from the estimated AOA. The method's performance was evaluated experimentally. The theoretical approach and experimental results are provided below.

The rest of this paper is organized as follows: Section 2 describes the effects of AOA fluctuations on the recorded video sequence, which are exploited here for the estimation of C_n^2 . Section 3 presents the proposed method for C_n^2 estimation from the image sequence. Section 4 discusses the feasibility of the method and estimation errors. Section 5 presents an experiment performed to examine the proposed method. In Section 6, the resulting C_n^2 values estimated by the proposed method are compared to those measured by a scintillometer. Conclusions are in Section 7.

2. ANGLE-OF-ARRIVAL FLUCTUATIONS

Variations in the refraction index induce multiple refractions of the wave propagating in the atmosphere. These refractions cause changes in the propagation direction. Consequently, the wavefront propagating from the object arrives at the optical aperture from a randomly changing angle. Wavefront AOA fluctuations have two main effects on the recorded video sequence: spatiotemporal movements (image dancing) and long-exposure blur. Image dancing occurs when the same object point is imaged at different locations across the frames. Long-exposure blur is caused by a summation of several shifted AOAs at each

frame exposure. In a sufficiently short frame exposure (up to a few milliseconds), a single AOA is recorded at each frame, so no long-exposure blur occurs. In a sufficiently long frame exposure (from a few hundred milliseconds), many AOAs are averaged at each frame, and form the same point-spread function at each of them, so no image dancing occurs. For the standard video frame exposures such as 16 ms in the National Television System Committee (NTSC) or 20 ms in the phase alternation line (PAL), per field, and typical atmospheric conditions, both phenomena will most likely degrade the video sequence in long-distance imaging. Important statistical characteristics that quantify these AOA effects are the variance and the spatial and temporal correlations. These characteristics are described below.

A. Angle-of-Arrival Variance

For typical imaging applications when the aperture diameter D is larger than turbulence inner scale ($D \gg l_0$), the AOA's single-axis variance for an infinite plane wave is given in radians by⁷

$$\sigma_\alpha^2 = 2.914D^{-1/3} \int_0^L C_n^2(z) dz, \quad l_0 \ll D \ll \sqrt{\lambda L}, \quad (1)$$

where the subscript α designates the deviation of the AOA in radians, L is the path length, and l_0 is the turbulence inner scale, which is of the order of millimeters.

Plane-wave approximation holds when the path difference from the source to different points on the optical aperture is negligible compared to the wavelength:

$$D \ll \sqrt{\lambda L}. \quad (2)$$

When $D \gg \sqrt{\lambda L}$, the spherical wave approximation should be used^{17,18}:

$$\sigma_\alpha^2 = 2.914D^{-1/3} \int_0^L C_n^2(z) \left(\frac{z}{L}\right)^{5/3} dz, \quad \sqrt{\lambda L} \ll D \ll L_0, \quad (3)$$

where L_0 is the turbulence outer scale. An IR camera with $D=20$ cm would require a path of at least 10 km for the plane-wave approximation to become valid. Equations (1) and (3) may be combined into the following expression:

$$\sigma_\alpha^2 = 2.914D^{-1/3} * \begin{cases} \int_0^L C_n^2(z) dz, & l_0 \ll D \ll \sqrt{\lambda L} \\ \int_0^L C_n^2(z) \left(\frac{z}{L}\right)^{5/3} dz, & \sqrt{\lambda L} \ll D \ll L_0 \end{cases}. \quad (4)$$

If we assume for simplicity of calculation, a constant C_n^2 along the imaging path (which may be commonly true for short horizontal imaging paths), we obtain a single-axis AOA variance:

$$\sigma_\alpha^2 = D^{-1/3} C_n^2 * \begin{cases} 2.914, & l_0 \ll D \ll \sqrt{\lambda L} \\ 1.1, & \sqrt{\lambda L} \ll D \ll L_0 \end{cases}. \quad (5)$$

For any particular combination of λ , L , D , and L_0 , which does not fit either spherical or plane-wave approximation

requirements, the coefficient in Eq. (5) may be calculated precisely.^{19,20} For the more general case, when C_n^2 varies along the imaging path, its value that satisfies Eq. (5) is referred to as path-averaged C_n^2 .

A wavefront angular shift of α radians at the optical aperture results in an image displacement of $\alpha \times \text{PFOV}^{-1}$ pixels, where PFOV is the pixel field of view. The image displacement single-axis variance σ_{img}^2 resulting from the AOA fluctuations would then be

$$\sigma_{\text{img}}^2 = \sigma_\alpha^2 \times \text{PFOV}^{-2}. \quad (6)$$

In a digital image, the units of σ_{img}^2 are pixels.²

B. Angle-of-Arrival Spatial and Temporal Correlation Properties

In geometrical optics approximations, wavefront distortions can be represented by Zernike polynomials.⁷ Each polynomial represents a different wavefront aberration such as tip, tilt, astigmatism, defocus. The AOA is represented by tip and tilt Zernike modes. Using the Zernike approach and the Von Karman refraction index model, the AOA spatial (angular) correlation function may be calculated for any particular D/L_0 ratio.¹⁹ It may be numerically obtained from Ref. 19 that, for a typical case of spherical wave approximation and $D/L_0 < 0.5$, the angular correlation scale for lateral AOA fluctuations is

$$\theta_C \approx DL^{-1}, \quad (7)$$

where θ_C is an angular distance between two objects with over an 85% AOA correlation. In most practical cases $L_0 > 2D$, thus the correlation is even higher. It is also termed the image-motion isoplanatic patch²⁰ and the isokinetic patch.²¹ The AOA temporal power spectrum was obtained theoretically and experimentally in several studies.¹⁹⁻²⁴ From the results obtained by Avila *et al.*²⁰ and Conan *et al.*,²² AOA fluctuations' temporal spectrum may be calculated. For the case of an outer scale much larger than the pupil diameter, an expression for the AOA correlation time is given by Eq. (5.12) in Ref. 22. It can be shown that 90% AOA temporal correlation, τ , is obtained for

$$\tau \approx DV^{-1}, \quad (8)$$

where V is the wind speed. For a nontransverse wind direction, the correlation would be even higher. Whenever the exposure time is less than the AOA correlation time, short-exposure imaging is considered. In this case, consecutive images are displaced one with respect to another, and spatiotemporal image dancing is observed. When the exposure time is bigger than the AOA correlation time, AOA variations during the exposure cause additional image blur. These properties will be considered regarding the feasibility of the proposed method in Section 4.

3. C_n^2 ESTIMATION FROM AN IMAGE SEQUENCE

As mentioned earlier, AOA fluctuations variance can be used for C_n^2 estimation. In this section, we propose a technique for automatic AOA variance estimation based on measuring the intensity variance in high-gradient regions.

A. Measuring Angle-of-Arrival Variance from the Intensity Variance

Image dancing results in sampling the image intensity on a varying grid. Within the isokinetic patch, the whole image is uniformly shifted relative to the detector. The intensity at location (m, n) in the k th image $I(m, n, k)$ can be related to the ideal image (as if no turbulence was present) $I_0(m, n)$ by

$$I(m, n, k) = I_0(m + \Delta x_{m,n,k}, n + \Delta y_{m,n,k}), \quad (9)$$

where $\Delta x_{m,n,k}$ and $\Delta y_{m,n,k}$ are the unknown horizontal and vertical shifts (within some isokinetic patch), respectively. For small shifts, we may use a first-order approximation of Eq. (9):

$$I(m, n, k) \approx I_0(m, n) + [I_X(m, n), I_Y(m, n)][\Delta x, \Delta y]^T, \quad (10)$$

where $[I_X(m, n), I_Y(m, n)]$ is the gradient vector, in which $I_X(m, n)$ and $I_Y(m, n)$ are the vertical and the horizontal derivatives of the ideal image at point (m, n) , respectively. This model is commonly used in gradient-based motion estimation techniques.²⁵ Next, we define the local temporal intensity variance $\sigma_I^2(m, n) \equiv \langle (I(m, n, k) - \bar{I}(m, n, k))^2 \rangle$, where $\langle \cdot \rangle$ designates an ensemble average over the discrete time index k . From Eq. (10), the local temporal intensity variance will be

$$\sigma_I^2(m, n) = [I_X(m, n), I_Y(m, n)][[\Delta x, \Delta y]^T [\Delta x, \Delta y]] \times [I_X(m, n), I_Y(m, n)]^T. \quad (11)$$

Since tip and tilt are uncorrelated,⁷ Δx and Δy are independent, and therefore $\langle \Delta x \Delta y \rangle = 0$. Image shifts along each axis are introduced by the corresponding AOA fluctuations of the propagating wave at the imaging pupil. Since AOA variances are equal for both axes [see Eq. (5)], we designate image shift variances along each axis, σ_x^2 and σ_y^2 , by $\sigma_{\text{img}}^2 \equiv \sigma_x^2 = \sigma_y^2$. Equation (11) now becomes

$$\sigma_I^2(m, n) = [I_X^2(m, n) + I_Y^2(m, n)]\sigma_{\text{img}}^2(m, n), \quad (12)$$

where $I_X^2(m, n) + I_Y^2(m, n)$ is the gradient square at the pixel (m, n) . Since the intensity temporal variance $\sigma_I^2(m, n)$ and the derivatives $I_X(m, n)$ and $I_Y(m, n)$ can be directly calculated from the image sequence, the turbulence-induced motion spatial variance $\sigma_{\text{img}}^2(m, n)$ may be obtained according to Eq. (12). Gradient computation can be done by filtering the image with a derivative mask, following a smoothing operation. Examples of such combined smoothing and derivative masks are $[-1 \ 8 \ 0 \ -8 \ 1]/12$ (Barron *et al.*²⁵) and $[1 \ 0 \ -1]/2$ (Simonchelli²⁶-order 3). Assuming a stationary scene during the sequence acquisition, the images are averaged to reduce noise, and the derivatives are computed. The averaging operation may cause blur, which may lead to an error in the gradient estimation for strong AOA fluctuations.

Equation (12) describes the connection between the intensity gradient, the intensity fluctuations, and the image displacement variance. The last, being determined essentially by the AOA fluctuations, allows for determining C_n^2 . Implementation of the proposed estimation of σ_{img}^2 from a real recorded image sequence is shown in Section 5.

B. C_n^2 Estimation

In Subsection 2.A, image dancing induced by optical turbulence is described [Eqs. (5) and (6)]. Intensity fluctuations caused by the image dancing are developed in Subsection 3.A. We may finally obtain the explicit formula for image intensity fluctuations as a function of C_n^2 . By substituting Eqs. (5) and (6) into Eq. (10), we obtain:

$$\sigma_I^2(m, n) = [I_X^2(m, n) + I_Y^2(m, n)]D^{-1/3}C_n^2L \times P \times \text{PFOV}^{-2}, \quad (13)$$

where P is defined according to Eq. (5):

$$P \equiv \begin{cases} 2.914 & \text{for } l_0 \ll D \ll \sqrt{\lambda L} \\ 1.1 & \text{for } \sqrt{\lambda L} \ll D \ll L_0 \end{cases}.$$

Then, having calculated the intensity variance for a certain point, $\sigma_I^2(m, n)$, C_n^2 can be estimated at locations with a high image gradient. From Eq. (13), we suggest the following C_n^2 estimator:

$$\tilde{C}_n^2(m, n) = ([I_X^2(m, n) + I_Y^2(m, n)]L \times P)^{-1} \text{PFOV}^2 D^{1/3} \sigma_I^2(m, n). \quad (14)$$

The finally estimated C_n^2 is the average of $\tilde{C}_n^2(m, n)$ over a number of pixels:

$$\tilde{C}_n^2 = \frac{1}{N} \sum_{m,n} \tilde{C}_n^2(m, n), \quad (15)$$

where N is the number of pixels used in the estimation process.

Since $\sigma_I^2(m, n)$ may contain other intensity fluctuation sources rather than turbulence-induced image dancing, only pixels with high-gradient values will produce a good C_n^2 estimation. In such points, intensity fluctuations will be dominated by image dancing rather than by imager's noise or intensity scintillations.

C. Summary of the Estimation Procedure

The estimation procedure consists of three major steps: intensity temporal variances calculation for all high-gradient points, AOA variance estimation from the intensity variance, and C_n^2 estimation from the AOA statistics.

If the recorded video is interlaced as in standard NTSC or PAL video formats, deinterlacing is first applied (the odd and the even fields are separated and considered as two consecutive images). In the first step, image gradient is obtained by applying horizontal and vertical derivative operations to the average image. Then, the square gradient is computed at each pixel. Pixels with high square gradient (as defined in Subsection 4.B) are chosen for the next step.

At each chosen point, the variance of the intensity temporal fluctuations is calculated. Having both intensity variance and spatial derivatives, C_n^2 is calculated according to Eq. (15). Obviously, for any chosen point in the image domain, the distance L to the corresponding object must be known. For an arbitrary set of images, the lack of this information may require rough distance estimation, which may impact the C_n^2 estimation accuracy. Deviation

between the C_n^2 estimations at different points may be used for accuracy evaluation.

4. FEASIBILITY AND ESTIMATION ERRORS

In this section, we consider the required conditions for a reliable C_n^2 estimation according to the proposed method.

A. Required Environmental Imaging Conditions

Generally speaking, to measure fluctuations of a certain signal, the sampling resolution should be much higher than the expected correlation length. Otherwise fluctuation reduction is expected due to averaging. Analogously, to efficiently measure AOA fluctuations, the pixel size and the exposure time are required to be much smaller than the isokinetic patch and the AOA correlation time, respectively. According to Eqs. (7) and (8), these requirements can be expressed, respectively, as

$$\begin{aligned} \text{PFOV} &\ll D/L, \\ T_e &\ll D/V, \end{aligned} \quad (16)$$

where T_e is the exposure time. D and T_e are usually known and fixed. PFOV is tunable for zoom-capable cameras. V and L are external parameters that are not commonly under control. The required conditions for these parameters according to Eq. (16) will then be

$$\begin{aligned} L &\ll D/\text{PFOV}, \\ V &\ll D/T_e. \end{aligned} \quad (17)$$

As may be seen from Subsection 5.A, the exposure time is $T_e \approx 15$ ms, and the narrowest PFOV is $\text{PFOV} \approx 40$ μrad . C_n^2 estimation with the proposed technique becomes feasible for transverse wind speeds slower than 13 m/s and a distance to the object shorter than 5 km.

B. Sufficient Gradient Magnitude

Temporal intensity variations can be accurately measured at high-gradient areas. A lack of such areas means no information, hence no blurring or dancing, may be extracted out of the images. Real-life images (produced in almost all imaging cases) are considered to include significant variations across the scene. Various studies have been carried out to examine the second-order statistics (spectrum) of real images.^{27,28} It was shown that the average power spectrum of natural images falls with a form of $1/f^\gamma$ where f is the spatial frequency and γ is approximately two. Such image properties imply the existence of intensity variations such as object edges, which are required in the proposed C_n^2 estimation process. Only pixels in regions of steep intensity variations are used in the proposed estimation process. In these regions, intensity variations caused by image dancing, σ_1^2 , should be much higher than the noise variance σ_N^2 , i.e., satisfy the condition $\sigma_N^2 \ll \sigma_1^2$, to obtain a low estimation error.

Intensity scintillations induced by turbulence may also contribute to the overall noise. Intensity fluctuations induced by the turbulence are traditionally calculated in terms of scintillation index.¹ It is easily obtained for the coherent case. However, in IR imaging, two effects must

be considered, noncoherent (polychromatic) wave and finite imager aperture. Tokovinin²⁹ gave a model to calculate scintillation effects for finite bandwidth and finite aperture. Recently, experimental results were presented regarding infrared image scintillations.³⁰

For simplicity, the total noise level was estimated from low-gradient regions in the image. In these regions, intensity temporal fluctuations result from image scintillations and noise rather than from image shifts, as in high-gradient regions.

C. Assumption for Isotropy

The proposed method is valid in the inertial range $l_0 \ll D \ll L_0$, where the wave structure function is assumed isotropic. Since L_0 scales with height h above ground according to $L_0 = 0.4h$, for a very close to earth imaging path, the isotropy assumption may not be valid. In such a case, the accuracy of estimation is considerably reduced. In our experimental setup where $D = 0.2\text{m}$, the isotropy assumption becomes marginal. However, it was discovered, in our experiments, that the differences between the vertical and the horizontal shifts (σ_y^2 and σ_x^2) were not significant.

5. EXPERIMENTAL EVALUATION OF THE PROPOSED C_n^2 ESTIMATION

Two comparative experiments were conducted. In these experiments, results of C_n^2 estimations from image sequences according to the proposed method were compared to C_n^2 measurements using a scintillometer. Video sequences of 500 frames were recorded, each for approximately half an hour. Scintillometer C_n^2 measurements were continuously recorded once a minute.

A. Setup

The setup included an IR camera, a personal computer (PC) setup for video acquisition, and a scintillometer connected to another PC for measurement recordings and control. The IR camera was the FOX720 manufactured by CONTROP³¹ Limited, with a 20 cm optical aperture diameter, a maximum focal length of 720 mm with a continuous zoom, and a $0.76^\circ \times 0.57^\circ$ narrowest field of view, corresponding to the PFOV of 40 μrad . The camera incorporates a Blue Fairy IR³² detector for the 3–5 μm spectral band with a 14 bit analog-to-digital detector readout and an 8-bit digital-to-analog detector readout for NTSC conversion. The NTSC output provided a 60 Hz field rate associated with a 16 ms exposure time (30 Hz interlaced frame rate).

C_n^2 measurements were performed with a surface layer scintillometer (SLS 20) working at a 670 nm wavelength with a 5 mrad beam divergence. The detector and the source were separated by 70 and 100 m in the first and in the second experiments, respectively. Measurements involved 60 s averaging. The scintillometer's effective C_n^2 measurement range was between 10^{-16} and $3 \times 10^{-12} \text{m}^{-2/3}$.

B. Environment

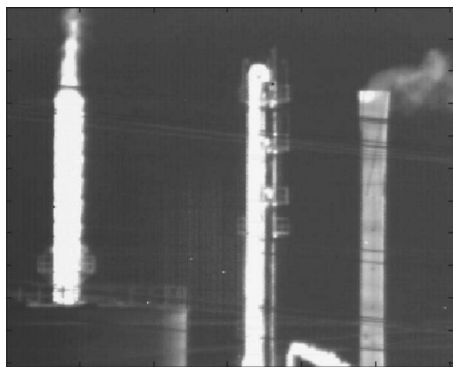
The first experiment took place in Haifa (Israel) on August 19, 2005, between 7 a.m. and 11 a.m. The imaging

path length was approximately 1000 m. C_n^2 values measured by a scintillometer were varying from 10^{-14} to $10^{-12} \text{ m}^{-2/3}$ during the experiment. Around 11 a.m., the turbulence was so strong that the induced image shifts could no longer be considered small due to the image smoothness properties. In this case, the small shift assumption made in Eq. (10) breaks down, and Eq. (12) becomes invalid. For this reason, in the last three measurements, the imaging path length was reduced to 100 m. As shown in Section 6, significant discrepancies between the measured and the estimated values of C_n^2 were observed. The possible reasons for these discrepancies were analyzed and another experiment was carried out to account for these discrepancies.

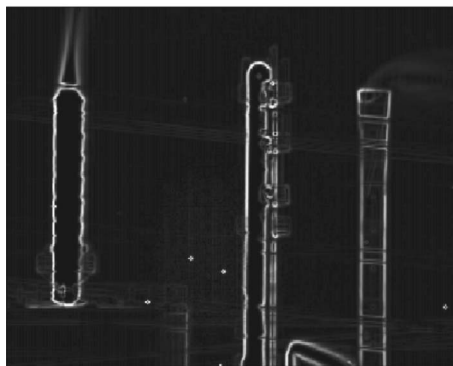
The second experiment took place in Beer Sheva (Israel) on September 23, 2005. The setup and the experiment goal were the same as in the first one. The major difference from the previous test was the significantly shorter imaging path (160 m only). The path was with equal height above ground, and the soil type under both the scintillometer and the camera imaging path was similar. Wind speed and additional weather parameters were recorded at the local weather station.³³ In both experiments, the camera was installed 1.5 m above the ground. The scintillometer's transmitter and receiver were both placed 1 m above the ground.

C. Region Choice for C_n^2 Estimation

As explained in Subsection 3.A, high-gradient value is required for a reliable C_n^2 estimation. The noise can be esti-

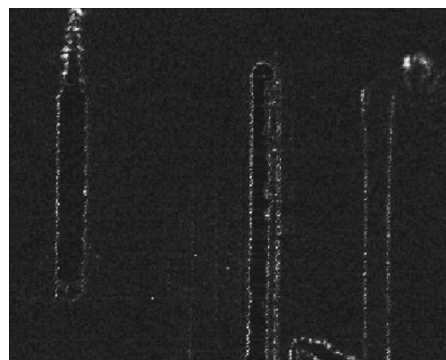


(a)

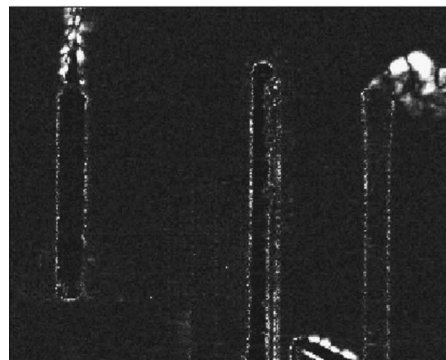


(b)

Fig. 1. Region choice for C_n^2 estimation: (a) averaged image; (b) gradient magnitude of the averaged image.



(a)



(b)



(c)

Fig. 2. Intensity fluctuations: (a) absolute difference between two consecutive odd fields; (b) absolute difference between two arbitrary odd fields; (c) STD of the intensity temporal fluctuations in the sequence of images.

mated from the intensity fluctuations within smooth uniform regions (where turbulence-induced image dancing is negligible).

Figure 1 shows an example for the region choice for the C_n^2 estimation for the first experiment. An average of 500 frames of a video sequence is presented in Fig. 1(a). The gradient magnitude of this image, $(I_x^2 + I_y^2)^{1/2}$, is shown in Fig. 1(b). The bright regions in Fig. 1(b) represent high-gradient areas.

Figure 2 presents the phenomenon of intensity temporal fluctuations due to image dancing. Figures 2(a) and 2(b) show the absolute difference between two consecutive odd fields and between two arbitrary (nonconsecutive) fields, respectively. Turbulence-induced intensity fluctuations are observed mainly in high spatial gradient areas.

Two consequent fields are less displaced, one with respect to the other. Therefore, intensity variations in the high-gradient regions are weaker in Fig. 2(a) relative to Fig. 2(b), since no motion correlation between movements in the two time-distant fields is expected. Figure 2(c) shows the standard deviation (STD) of the intensity temporal fluctuations in the sequence of images calculated at each pixel. Since high STD occurs at high-gradient regions, this temporal STD image mainly visualizes the areas of the spatial edges in the image (i.e., high temporal fluctuations correspond to high spatial gradients). In such areas, the intensity temporal variations are determined by turbulence-induced image dancing rather than by noise ($\sigma_N^2 \ll \sigma_I^2$). We choose these areas (pixels) for C_n^2 estimation and proceed to the next step.

6. RESULTS

For each pixel chosen in the previous step, intensity temporal variance $\sigma_I^2(m, n)$ was calculated as described in

Table 1. First Experiment^a

| Time of Day H:MM | C_n^2 Measured ($m^{-2/3}$) | C_n^2 Estimated ($m^{-2/3}$) | Estimation Relative Error (No Unit) |
|---------------------|---------------------------------------|--|--|
| 7:30 | 2.1×10^{-14} | 2.6×10^{-14} | 0.16 |
| 8:00 | 3.4×10^{-14} | 2.9×10^{-14} | 0.14 |
| 8:39 | 1.2×10^{-13} | 5.5×10^{-14} | 0.13 |
| 8:53 | 6.7×10^{-13} | 1.3×10^{-13} | 0.17 |
| 9:02 | 3.5×10^{-13} | 7.1×10^{-13} | 0.29 |
| 9:14 | 1.2×10^{-12} | 1.9×10^{-13} | 0.13 |
| 9:36 | 1.2×10^{-12} | 3.1×10^{-13} | 0.19 |
| 9:47 | 1.4×10^{-12} | 2.2×10^{-13} | 0.24 |
| 10:06 | 1.2×10^{-12} | 3.6×10^{-13} | 0.2 |
| 10:12 | 1.1×10^{-12} | 1.3×10^{-12} | 0.19 |
| 10:35 | 1.6×10^{-12} | 2.6×10^{-12} | 0.35 |
| 10:58 | 1.7×10^{-12} | 2.9×10^{-12} | 0.28 |

^aComparison between C_n^2 values estimated from image sets (third column) and those measured with a scintillometer (second column) at different times.

Table 2. Second Experiment^a

| Time of Day H:MM | C_n^2 Measured ($m^{-2/3}$) | C_n^2 Estimated ($m^{-2/3}$) | Estimation Relative Error (No Unit) |
|---------------------|---------------------------------------|--|--|
| 8:40 | 1.6×10^{-13} | 1.5×10^{-13} | 0.29 |
| 8:48 | 2.1×10^{-13} | 3.2×10^{-13} | 0.21 |
| 9:24 | 2.2×10^{-13} | 3.6×10^{-13} | 0.11 |
| 9:30 | 2.3×10^{-13} | 1.9×10^{-13} | 0.12 |
| 9:44 | 2.1×10^{-13} | 2.3×10^{-13} | 0.14 |
| 9:50 | 2.4×10^{-13} | 1.8×10^{-13} | 0.13 |
| 10:07 | 4.0×10^{-13} | 2.4×10^{-13} | 0.12 |
| 10:11 | 3.4×10^{-13} | 3.8×10^{-13} | 0.18 |
| 10:24 | 4.5×10^{-13} | 3.4×10^{-13} | 0.28 |
| 10:46 | 2.3×10^{-13} | 4.4×10^{-13} | 0.25 |
| 10:57 | 4.8×10^{-13} | 4.1×10^{-13} | 0.15 |
| 11:11 | 4.5×10^{-13} | 6.6×10^{-13} | 0.23 |

^aComparison between C_n^2 values estimated from image sets (third column) and those measured with a scintillometer (second column) at different times.

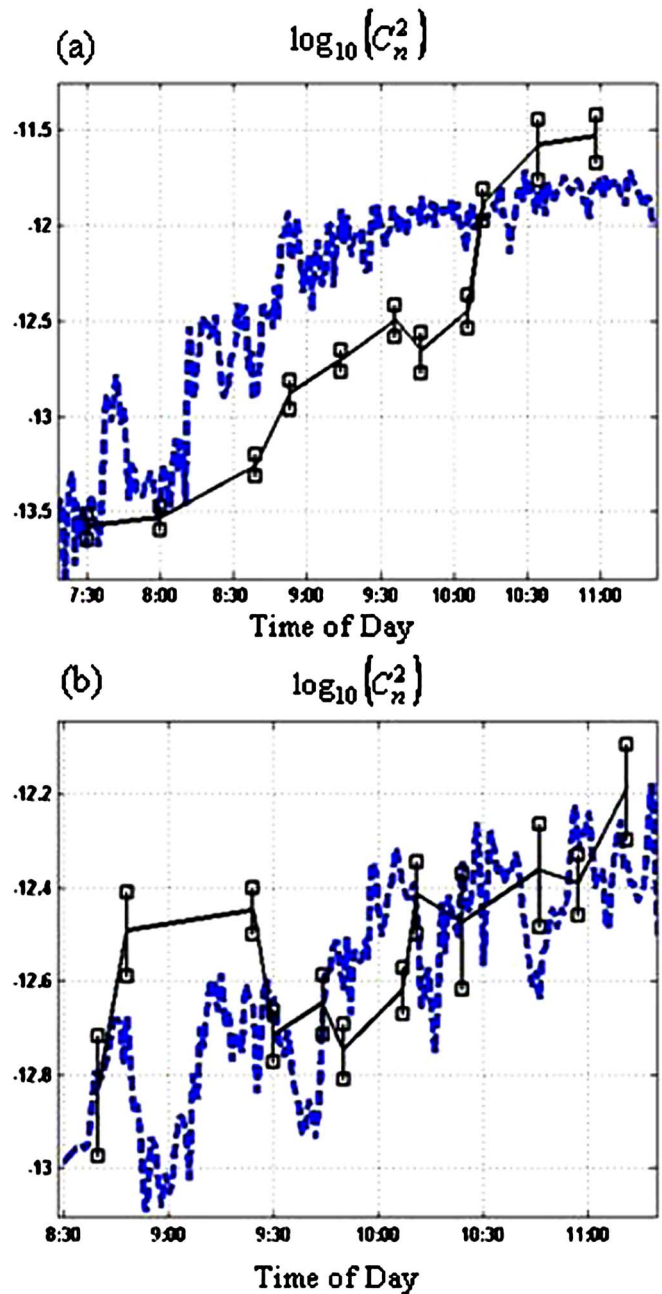


Fig. 3. (Color online) Graphic comparison between values of C_n^2 estimated from the video sequence (solid curve) and C_n^2 values measured by a scintillometer (dashed curve), according to the tables. (a) Results of first experiment according to Table 1. (b) Results of second experiment according to Table 2.

Subsection 3.A. Next, a C_n^2 value was obtained for each pixel according to Eq. (14), allowing for the spherical wave case. The average of the C_n^2 values and their STD were calculated from the acquired image sets. The averaged C_n^2 value is considered the path-averaged turbulence strength for a given set of images. The STD of estimated C_n^2 values is used for estimation error assessment. A comparison between estimated C_n^2 values and those measured with the scintillometer is presented in Tables 1 and 2 for the first and the second experiments, respectively. In each table, each row presents the results obtained from a recorded image sequence at a certain time, specified in the

first column. The second column, measured C_n^2 , consists of values obtained by the scintillometer. The third column, estimated C_n^2 consists of values estimated by the proposed method. The relative error (last column) is the standard deviation of the C_n^2 values obtained from different pixels normalized by the mean (estimated) value.

Figure 3 contains two graphs, (a) and (b), showing the results of the first and the second experiments, respectively. Each presents a graphic comparison between the C_n^2 values measured by a scintillometer and those estimated from the image sequences according to the proposed method, at different times. High similarity in behavior is obtained between the two techniques in both experiments, as the values of C_n^2 increase with the time of the day. However, in the first experiment, significant discrepancies are found between the measured and the estimated C_n^2 values. These discrepancies can be explained as follows. The scintillometer was installed on a gravel yard, low above ground, with the distance of 70 m between the source and the receiver. Hence, it measured local C_n^2 values, whereas the C_n^2 estimated from the images is associated with path-averaged turbulence. The imaging path was partially above vegetated fields, having lower C_n^2 . Furthermore, the points used for C_n^2 estimation were objects, dozens of meters above the ground. Thus, path-averaged C_n^2 is expected to be smaller as a result of the different soil type and the height above ground.

In the second experiment, these effects were eliminated using a significantly shorter imaging path length. Results of this experiment are presented in Table 2 and Fig. 3(b). A much better agreement between the measured and the estimated C_n^2 values is observed.

7. CONCLUSIONS

A method for an automatic estimation of the turbulence structure constant C_n^2 from a sequence of images is proposed. The method is based on locating high-gradient features in the image and measuring their turbulence-induced spatial shifts throughout the image sequence. These displacements are associated with varying wavefront angles of arrival at the optical aperture. Whenever AOAs' root mean square is estimated, a path-averaged C_n^2 may be obtained. Knowledge of the distance to the object and the pixel's FoV are required in the estimation process.

The proposed C_n^2 estimation technique is mostly applicable for short distances, since for longer imaging paths, anisoplanatic effects lead to AOA averaging. With commercially available cameras with a PFOV of the order of ~ 50 μ rad and a pupil diameter of ~ 10 cm, the effective distances are as short as several hundreds of meters to several kilometers only. Another difficulty in the proposed technique is the AOA correlation time, which may be as short as just a few milliseconds for reasonable wind speeds. This difficulty is eliminated when the imaging direction is parallel to the wind speed, or when the wind speed is low (~ 1 m/s); otherwise a short-exposure camera may be required.

The major value of the proposed method is the automatic use of only the available video sequence without the

need for specific equipment and without the need to image specific structures in the scene (such as a point source or a perfect edge as demonstrated by other techniques). The proposed method was examined experimentally by comparing its C_n^2 estimation results with results obtained with a scintillometer. Relatively small differences in the C_n^2 values have been found between the two methods.

ACKNOWLEDGMENTS

We thank Adam Devir for his helpful support and advice and for providing the instrumentation that was necessary for this research. We also thank Leah Moshe and Eyal Hollander for participating in the experiments.

The corresponding author Y. Yitzhaky may be reached at tel: 972-8-6461840; fax: 972-8-6479494; e-mail: itzik@ee.bgu.ac.il.

REFERENCES

1. V. Tatarski, *Wave Propagation in a Turbulent Medium* (Dover, 1967).
2. R. Tyson, *Principles of Adaptive Optics* (Academic, 1991).
3. N. S. Kopeika, *System Engineering Approach to Imaging* (SPIE, 1998), Chap. 18.
4. Y. Yitzhaky, I. Dror, and N. S. Kopeika, "Restoration of atmospherically blurred images according to weather predicted atmospheric modulation transfer function (MTF)," *Opt. Eng. (Bellingham)* **36**, 3064–3072 (1997).
5. D. R. Gerwe and M. A. Plonus, "Superresolved image reconstruction of images taken through the turbulent atmosphere," *J. Opt. Soc. Am. A* **15**, 2620–2628 (1998).
6. D. G. Sheppard, B. R. Hunt, and M. W. Marcellin, "Iterative multiframe superresolution algorithms for atmospheric turbulence-degraded imagery," *J. Opt. Soc. Am. A* **15**, 978–992 (1998).
7. M. Roggemann and B. Welsh, *Imaging Through Turbulence* (CRC, 1996), Chap. 6.
8. R. A. Johnston, N. J. Wooder, F. C. Reavell, M. Bernhardt, and C. Dainty, "Horizontal scintillation detection and ranging $C_n^2(z)$ estimation," *Appl. Opt.* **42**, 3451–3459 (2003).
9. R. W. Wilson, "SLODAR: measuring optical turbulence with a Shack-Hartmann wavefront sensor," *Mon. Not. R. Astron. Soc.* **337**, 103–108 (2002).
10. G. D. Love, C. N. Dunlop, S. Patrick, C. D. Saunter, R. W. Wilson, and C. Wright, "Horizontal turbulence measurements using SLODAR," in *Atmospheric Optical Modeling, Measurement, and Simulation*, S. M. Doss-Hammel and A. Kohnle, eds., Proc. SPIE **5891**, 27–32 (2005).
11. G. G. Gimmestad and D. W. Roberts, "Laser remote sensing of atmospheric turbulence," in *Laser Systems Technology*, W. E. Thompson and P. H. Merritt, eds., Proc. SPIE **5087**, 167–172 (2003).
12. V. Kornilov and A. Tokovinin, "Measurement of the turbulence in the free atmosphere above Mt. Maidanak," *Astron. Rep.* **45**, 395–408 (2001).
13. K. R. Weiss-Wrana, "Turbulence statistics applied to calculate expected turbulence-induced scintillation effects on electro-optical systems in different climatic regions," in *Atmospheric Optical Modeling, Measurement, and Simulation*, S. M. Doss-Hammel and A. Kohnle, eds., Proc. SPIE **5891**, 117–128 (2005).
14. F. D. Eaton, "Recent developments of optical turbulence measurement techniques," in *Atmospheric Propagation II*, B. F. Andresen and G. F. Fulop, eds., Proc. SPIE **5793**, 68–77 (2005).
15. A. Consortini, C. Innocenti, and S. Ceccarelli, "Measuring the refractive index gradient of the atmosphere," in *Optics*

- in *Atmospheric Propagation and Adaptive Systems VIII*, K. Stein and A. Kohnle, eds., Proc. SPIE **5981**, 96–104 (2005).
16. M. J. Vilcheck, A. E. Reed, H. R. Burris, W. J. Scharpf, C. Moore, and M. R. Suite, "Multiple methods for measuring atmospheric turbulence," in *Free-Space Laser Communication and Laser Imaging II*, J. C. Ricklin and D. G. Voelz, eds., Proc. SPIE **4821**, 300–309 (2002).
 17. L. Andrews and R. Phillips, *Laser Beam Propagation through Random Media*, 2nd ed. (SPIE 2005), Chap. 6.5.
 18. L. Andrews, *Field Guide to Atmospheric Optics* (SPIE Field Guides, 2004), Vol. FG02, p. 29.
 19. M. Belenkii, J. M. Stewart, and P. Gillespie, "Turbulence-induced edge image waviness: theory and experiment," *Appl. Opt.* **40**, 1321–1328 (2001).
 20. R. Avila, A. Ziad, J. Borgnino, F. Martin, A. Agabi, and A. Tokovinin, "Theoretical spatio-temporal analysis of angle of arrival induced by atmospheric turbulence as observed with grating scale monitor experiment," *J. Opt. Soc. Am. A* **14**, 3070–3082 (1997).
 21. A. Ghedina, R. Ragazzoni, and A. Baruolo, "Isokinetic patch measurements on the edge of the Moon," *Astron. Astrophys., Suppl. Ser.* **130**, 561–566 (1998).
 22. R. Conan, J. Borgnino, A. Ziad, and F. Martin, "Analytical solution for the covariance and for the coherence time of the angle of arrival of a wave front corrugated by atmospheric turbulence," *J. Opt. Soc. Am. A* **17**, 1807–1818 (2000).
 23. J. Conan, G. Rousset, and P. Madec, "Wave-front temporal spectra in high-resolution imaging through turbulence," *J. Opt. Soc. Am. A* **12**, 1559–1570 (1995).
 24. F. Roddier, M. J. Northcott, J. E. Graves, and D. L. McKenna, "One-dimensional spectra of turbulence-induced Zernike aberrations: time-delay and isoplanicity error in partial adaptive compensation," *J. Opt. Soc. Am. A* **10**, 957–965 (1993).
 25. J. L. Barron, D. J. Fleet, S. S. Beauchemin, and T. A. Burkitt, "Performance of optical flow techniques," in *Proceedings of the Computer Vision and Pattern Recognition Conference* (IEEE, 1992), pp. 236–242.
 26. E. Simonchelli, "Design of multidimensional derivative filters," in *Proceedings of First IEEE Conference on Image Processing* (IEEE, 1994), Vol. 1, pp. 790–793.
 27. G. J. Burton and T. R. Moorehead, "Color and spatial structure in natural scenes," *Appl. Opt.* **26**, 157–170 (1987).
 28. D. J. Fields, "Relations between the statistics of natural images and the response properties of cortical cells," *J. Opt. Soc. Am. A* **4**, 2379–2394 (1987).
 29. A. Tokovinin, "Polychromatic scintillation," *J. Opt. Soc. Am. A* **20**, 686–689 (2003).
 30. I. G. E. Renhorn, T. Svensson, G. Carlsson, S. Cronström, and G. D. Boreman, "Infrared image scintillation: comparison of modeling and measurement," *Opt. Eng. (Bellingham)* **45**, 016001 (2006).
 31. CONTROP, FOX720 camera specifications, 2006, <http://www.controp.co.il/PRODUCTS/>.
 32. SCD, Blue Fairy detector specifications, 2006, <http://www.scd.co.il/blue.asp>.
 33. Weather Station, Department of Geography and Environmental Development, Ben Gurion University of the Negev, Beer Sheva, Israel, 2006, http://www.epifdb.bgu.ac.il/Meteorologic/JSP_NoSecure_Eng/ShowDataInput_Eng.jsp.